MDPI

Article

Deep-Learning-Based Estimation of the Spatial QRS-T Angle From Reduced-lead ECGs

Ana Santos Rodrigues[1,†], Rytis Augustauskas[2], Mantas Lukoševičius[3], Pablo Laguna[4,5], and Vaidotas Marozas[1,6]

[1] Biomedical Engineering Institute, Kaunas University of Technology, 51423 Kaunas, Lithuania
[2] Department of Automation, Kaunas University of Technology, 51367 Kaunas, Lithuania
[3] Faculty of Informatics, Kaunas University of Technology. Kaunas, Lithuania
[4] Biomedical Signal Interpretation and Computational Simulation (BSICoS) Group, Aragón Institute of Engineering Research (I3A), IIS Aragón, University of Zaragoza, 50018 Zaragoza, Spain
[5] Biomedical Research Networking Center (CIBER), 50018 Zaragoza, Spain
[6] Faculty of Electrical and Electronics Engineering, Kaunas University of Technology, 51367 Kaunas, Lithuania
* Correspondence: Ana Santos Rodrigues (ana.rodrigues@ktu.lt); Tel.: +370-37-300-528.

Abstract: The spatial QRS-T angle is an important indicator in stratifying the risk of sudden cardiac death. This indicator is usually calculated from Frank or 12 lead ECG electrode systems, which are quite uncomfortable for the user in ambulatory monitoring applications. Objective: To develop a method for the estimation of the spatial QRS-T angle from a reduced set of ECG leads. Approach: The estimator is based on a deep learning neural network consisting of automatic feature extraction and regression layers. The training efficiency of the algorithm is increased by proposing a composite loss function taking into account the angle itself and its quadrant in a coordinate system. A gradual reduction of ECG leads from a publicly available dataset of clinical ECG recordings in PTB XL (21837) was used for training, validation, and testing. Results: The results suggest that a machine-learning-based estimation of spatial QRS-T angle from a few frontal and at least one precordial leads is possible with the accuracy (???) sufficient for the detection of abnormal QRS-T angles. A good compromise between error and comfortability was achieved by using the following ECG leads: I, II, aVF, V2. Significance: The study demonstrates that the proposed approach could be of value for prolonged ambulatory monitoring of patients using wearable patch electrodes as used with miniature ECG devices. Chronic patients with cardiac and kidney disease could potentially benefit from this technology.

Keywords: wearable devices; unobtrusive monitoring; machine learning; regression.

Citation: Lastname, F.; Lastname, F.; Lastname, F. Title. *Sensors* **2022**, *1*, 0. https://doi.org/

Received:
Accepted:
Published:

1. Introduction

Despite recent advances in treating cardiovascular diseases, sudden cardiac death (SCD) remains the leading cause of mortality, accounting for approximately 20% of all deaths in western societies [1,2]. Dangerous arrhythmias precipitated by abnormalities in ventricular repolarization often precede SCD [3–5]. Various markers of abnormal repolarization in the electrocardiogram (ECG) have been proposed to stratify the risk of SCD, including changes in ST-segment [6] and QT interval lengthening []. However, those that evaluate the similarity between the direction of depolarization and repolarization, such as the QRS-T angle, are deemed the most promising [7–9]. Unfortunately, QRS-T angle estimation is restricted to clinical settings. The conventional approach for QRS-T angle estimation [7,10] is uncomfortable for patients as it requires a standard 12-lead ECG, hindering the possibility of harnessing the diagnostic value of the QRS-T angle for the early detection of dangerous cardiac events in out-of-hospital settings. Methods to estimate the QRS-T angle with a set of reduced-lead ECGs would, therefore, be of clinical importance. Such methods could be deployed in consumer healthcare devices and facilitate ambulatory monitoring of the QRS-T angle in populations at risk of life-threatening cardiac events.

Thus far, the QRS-T angle is estimated exclusively from three orthogonal leads, either the vectorcardiogram (VCG) [7] or orthogonalized 12-lead ECGs [10], that depict the electrical activity of the heart in the *xyz* plane. In the absence of Frank's lead system, the VCG is regularly reconstructed from the standard 12-lead ECG by applying one of the various mathematical transformations that convert 12-lead ECGs into a set of three orthogonal leads [11–13]. Registration of a 12-lead ECG, or even Frank's VCG, requires the patient to use eight or ten electrodes [12], causing considerable discomfort. Configuring eight-to-ten electrodes as specified in Holter monitors is usually an intricate task for the ordinary patient, making it unfeasible even to request patients to set up such devices for intermittent monitoring of the QRS-T angle. Conversely, consumer healthcare devices, designed to ameliorate patient discomfort, are compact, practical, and easy to configure. However, the number of ECG leads registered by consumer healthcare devices is limited to a few frontal with one-to-two precordial leads. These sets of leads are insufficient to reconstruct the VCG, thus precluding the employment of any of the existing methods for QRS-T angle estimation.

The QRS-T angle, classified as spatial or frontal [7], shows good prognosis for SCD [8], with increased values linked to various cardiac dysfunctions [14,15] and a higher risk of SCD [8]. The spatial QRS-T angle is defined as the angle between the QRS and T wave vectors in the *xyz* plane, whereas the frontal is the projection of the spatial angle in the *xy* (frontal) plane. The frontal angle, albeit less diagnostically powerful than the spatial angle [16], continues to be an attractive marker of repolarization abnormalities [8]. Although theoretically, the frontal angle could be calculated from frontal leads ECGs [17] acquired with consumer healthcare devices, some precordial leads are essential to derive leads *XY* with acceptable accuracy [12,13], again limiting any prospects of using the frontal QRS-T angle for ambulatory monitoring of dangerous cardiac events.

Deep neural networks have demonstrated tremendous capabilities to extract key data insights from sets of reduced-lead ECGs instead of the standard 12-leads. For instance, 1D convolutional neural networks (CNNs) have been shown to detect arrhythmias [18,19] and even sleep apnea [20,21] with up to 97.1% accuracy [21] in single-lead ECGs. CNNs have also reconstructed the standard 12-lead ECG from only three measured leads [22,23]. The ostensible potential of deep learning models has motivated us to investigate whether it is possible to estimate the spatial QRS-T angle using a set of reduced-lead ECGs. We hypothesize that, by using 12-lead ECGs, we can derive QRS and T vectors required to compute the spatial QRS-T angle from the VCG and train the model to associate these vectors with a specific subset of ECG leads.

This study presents a 1D convolutional neural network (CNN1D) to measure the spatial QRS-T angle from signal-averaged heartbeats of reduced-lead ECGs. Since the spatial location of QRS and T vectors is largely dependent on the cardiac conduction axis, we design the model to return the coordinates of both vectors as output. Our study introduces a personalized composite loss function that uses both the QRS-T angle and the Euclidean distance between the vectors to guide the model throughout the 3D space. The model is developed on the *PTB-XL* [24] dataset, the largest publicly available database of clinical 12-lead ECG recordings. We investigate the performance of our model in sets of ECG leads that can conveniently be recorded with patch-based consumer healthcare devices. Lastly, we explore the feasibility of measuring the spatial QRS-T angle from solely frontal leads, aiming to understand the future challenges of deep-learning-based QRS-T angle estimation for out-of-hospital settings. To our knowledge, this is the first study to examine the feasibility of estimating the QRS-T angle from reduced-lead ECGs.

This article is organized as follows. Section 2 and 3 describe the conventional and the proposed deep-learning-based approaches for QRS-T angle estimation. Section 4 discloses information about the training and validation dataset, including the data preparation and labeling procedures. Section 5 defines the investigative methodology and performance evaluation. Finally, section 6 presents the results, followed by a discussion and conclusions in sections 7 and 8.

2. Conventional Approach for QRS-T Angle Estimation

The spatial QRS-T angle is estimated from a set of three orthogonal leads, obtained either by applying orthogonalization methods to 12-lead ECGs [10,25] or, conventionally, the VCG. The VCG, composed of leads XYZ, reflects the electrical activity of the heart in the orthogonal planes [26]: frontal (xy), transverse (xz), and sagittal (yz). In essence, the VCG depicts heartbeats as a trajectory of XYZ leads over time,

$$\vec{\boldsymbol{v}}(t) = \big(x(t), y(t), z(t)\big), \tag{1}$$

in which the depolarization (QRS) and repolarization (T) processes of a heartbeat are represented as two loops:

$$\vec{\boldsymbol{v}}_{QRS}(t) = \vec{\boldsymbol{v}}(t) - \vec{\boldsymbol{v}}_0\,, \;\; \forall t \in \{t_{QRS_o}, \ldots, t_{QRS_e}\}, \tag{2}$$

$$\vec{\boldsymbol{v}}_{T}(t) = \vec{\boldsymbol{v}}(t) - \vec{\boldsymbol{v}}_0\,, \;\; \forall t \in \{t_{T_o}, \ldots, t_{T_e}\}, \tag{3}$$

where t_{QRS_o}, t_{T_o}, t_{QRS_e}, and t_{T_e} are the respective onset and offset of QRS and T loops. Following the guidelines in [27], the origin of both loops $\vec{\boldsymbol{v}}_0$ is estimated as:

$$\vec{\boldsymbol{v}}_0 = \text{median}\big(\vec{\boldsymbol{v}}(t)\big)\,, \; \forall t \in \{t_{QRS_o} - \tau_0, \ldots, t_{QRS_o}\} \text{ and } \tau_0 = 25\,\text{ms}. \tag{4}$$

Since inaccuracies in heartbeat delineation can generate significant errors in the estimation of QRS-T angle, the onsets t_{QRS_o}, t_{T_o}, and offsets t_{QRS_e}, t_{T_e} are adjusted as instructed in [27].

The spatial QRS-T angle measures the dissimilarity between the orientation of the QRS and T loops in the xyz space and is calculated as:

$$\alpha = \arctan\left(\frac{\big\|\vec{\boldsymbol{u}}_{QRS} \times \vec{\boldsymbol{u}}_t\big\|}{\vec{\boldsymbol{u}}_{QRS} \cdot \vec{\boldsymbol{u}}_T}\right), \tag{5}$$

where $\vec{\boldsymbol{u}}_{QRS}$ and $\vec{\boldsymbol{u}}_T$ are vectors that depict the orientation of QRS and T loops. The loop orientation is most commonly defined in the time instance $t = t_m$ where the maximum magnitude [7] of $\vec{\boldsymbol{v}}_{QRS}(t)$ and $\vec{\boldsymbol{v}}_T(t)$ is verified:

$$\vec{\boldsymbol{u}}_{QRS} = \vec{\boldsymbol{v}}_{QRS}(t_{QRS_m}) = \underset{\vec{\boldsymbol{v}}_{QRS}(t)}{\arg\max}\big(\big\|\vec{\boldsymbol{v}}_{QRS}(t)\big\|\big), \tag{6}$$

$$\vec{\boldsymbol{u}}_{T} = \vec{\boldsymbol{v}}_{T}(t_{T_m}) = \underset{\vec{\boldsymbol{v}}_{T}(t)}{\arg\max}(\|\vec{\boldsymbol{v}}_{T}(t)\|). \tag{7}$$

Although intuitive, defining the loop spatial orientation as the maximum magnitude vectors at a single-time instance is an oversimplification, as it assumes that the morphology of the QRS and T loops is unambiguous enough to have a well-defined spatial orientation. In abnormal ECGs, the spatial orientation of the loops, in particular the QRS loop, is too complex to be represented by a vector in a single instance in time. In fact, estimation of the QRS-T angle using $\vec{\boldsymbol{v}}_{QRS}(t_{QRS_m})$ and $\vec{\boldsymbol{v}}_T(t_{T_m})$ has been associated with higher errors and poorer reproducibility [28], namely in unhealthy ECGs.

A routinely employed strategy to tackle the problem of defining the underlying spatial orientation of the QRS loop is the *total cosine R-to-T* (TCRT) [10] method. TCRT defines the QRS-T angle as the average cosine of all angles between $\vec{\boldsymbol{v}}_T(t_{T_m})$ and every vector within the QRS loop that exceed 70% of the maximum vector magnitude $\vec{\boldsymbol{v}}_{QRS}(t_{QRS_m})$. However, computation of an averaged angle can become problematic in sets of reduced-lead ECGs that do not carry the same amount of spatial information as the VCG (see Section 3.2). Consequently, we adopt a strategy analogous to TCRT, but instead of deriving the average cosine, we define $\vec{\boldsymbol{u}}_{QRS}$ and $\vec{\boldsymbol{u}}_T$ as the average of all vectors exceeding 70% of the maximum vector magnitude within the corresponding loops:

$$\vec{\boldsymbol{u}}_{QRS} = \underset{t'}{\text{mean}}\big(\vec{\boldsymbol{v}}_{QRS}(t')\big)\,, \;\; \text{where} \;\; \big\|\vec{\boldsymbol{v}}_{QRS}(t')\big\| \geq 0.7\,\vec{\boldsymbol{v}}_{QRS}(t_{QRS_m}), \tag{8}$$

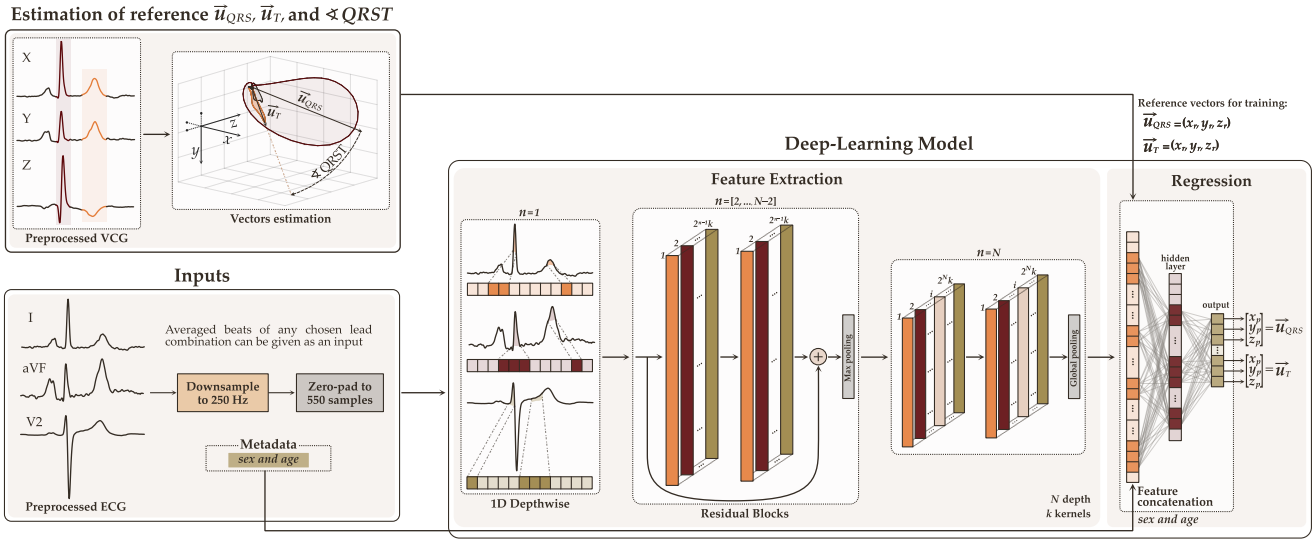

Figure 1. Overview of the proposed deep learning model for estimation of QRS-T angle using reduced-lead ECGs. The model is composed of two parts: feature extraction and regression.The reference vectors $\vec{u}_{QRS}$ and $\vec{u}_T$ and angle α are computed from preprocessed VCGs. A set of reduced-leads heartbeats are fed as an input for feature extraction.

$$\vec{u}_T = \underset{t'}{\text{mean}}\left(\vec{v}_T(t')\right), \text{ where } \left\|\vec{v}_T(t')\right\| \geq 0.7\,\vec{v}_T(t_{T_m}). \tag{9}$$

3. Deep-Learning-Based Approach for QRS-T Angle Estimation

We propose a deep learning model to estimate the spatial QRS-T angle using a set of reduced-lead ECG. Essentially, the model extracts high-level features from a set of signal-averaged heartbeats parsed as input and maps these features to the three coordinates of $\vec{u}_{QRS}$ and $\vec{u}_T$, i.e., $\vec{u}_{QRS} = (x_{QRS}, y_{QRS}, z_{QRS})$ and $\vec{u}_T = (x_T, y_T, z_T)$, returning the two vectors as the output.

Using 12-lead ECGs, we can compute the reference (target) VCG vectors $\vec{u}_{QRS}$ and $\vec{u}_T$ using the conventional approach described by equations (8) and (9), and train the model to produce the target $\vec{u}_{QRS}$ and $\vec{u}_T$ from specific subsets of ECG leads. The QRS-T angle can then be calculated as the angle between the estimated vectors, $\widehat{\vec{u}}_{QRS}$ and $\widehat{\vec{u}}_T$, as per equation (5). The model is purposely designed to extract the vectors instead of the angle directly to harness the available spatial information for training the model (see Section 3.2). Figure 1 presents an overview of our deep-learning-based approach. From this point onwards, the circumflex symbol denotes variables estimated by the model: $\widehat{\vec{u}}_{QRS}$, $\widehat{\vec{u}}_T$, and the QRS-T angle $\widehat{\alpha}$ between them; whereas $\vec{u}_{QRS}$ and $\vec{u}_T$ are the VCG target vectors and α is the angle between them.

3.1. Deep Learning Model Architecture

A 1D convolutional neural network (CNN1D) with a regression output is the baseline architecture for our proposed model. The model comprises two main networks: feature extraction and regression. Since distinct subsets of ECG leads may entail different configurations, we first describe the baseline architecture of our model, and then detail hyperparameters tuning.

3.1.1. Feature Extraction Network

The feature extraction network is composed of D blocks of layers connected sequentially. Each block consists of two *"layer structures"*, except the first block, which only includes one. Each *layer structure* is a sequence of a full 1D convolutional layer with k

kernels of size 3×1 and a stride of 1, followed by layer normalization, and activation (Figure 2–**b**). Layer normalization balances the data to have mean close to 0.0 and standard deviation close to 1.0 using scale and shift parameters that are trainable for each feature map. Leaky Rectified Linear Unit (Leaky ReLU) with the negative slope coefficient coefficient of 0.1 is the chosen activation function. In the first block, a depthwise convolutional layer is employed instead of a full convolution (Figure 2–**a**). A depthwise convolution allows the model to derive lead-specific features separately, as each lead can carry relevant information on the position of each coordinate of $\vec{\boldsymbol{u}}_{QRS}$ and $\vec{\boldsymbol{u}}_{T}$. Because depthwise convolution layers generate feature maps for each individual lead, the initial number of kernels k is distributed across all leads: $\frac{k}{j-1}$, where j is the number of input leads. This avoids having a larger feature map in the first layer than in the second.

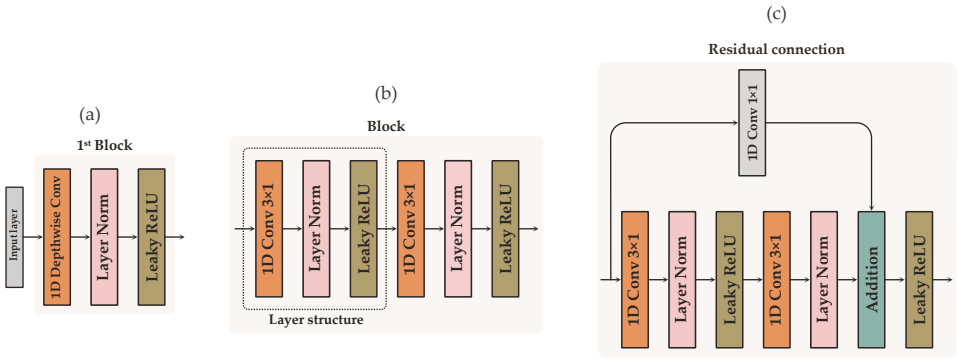

Figure 2. Detailed representation of the three types of blocks employed in the feature extraction network: **(a)** first block, **(b)** the last block, and **(b)** blocks with residual connections.

Residual connections (Figure 2–**c**) are introduced from the second block $d = 2$ to the $d = D^{th} - 2$ block to maintain data flow throughout the network and avoid gradient degradation during training. Prior to addition, 1×1 convolution is used to equalize the number of feature maps between the layers. The number of filters increases by a factor of 2 in every residual block. Abstraction of the most significant features is performed with *max pooling* at the end of blocks $d = [2{:}D-1]$, whereas *global average pooling* is implemented to finalize the last block $d = D$ of the feature extraction network.

To avoid overfitting, *dropout* with a probability of 0.25 is applied after feature extraction. Layer normalization also aids in preventing overfitting. It introduces noise by mixing the data after every epoch and shuffling the samples given in every minibatch.

3.1.2. Regression Network

The resultant feature map is connected to the regression network, which learns to associate the abstracted features with six neurons: one for each of the three coordinates of $\widehat{\vec{\boldsymbol{u}}}_{QRS} = (\hat{x}_{QRS}, \hat{y}_{QRS}, \hat{z}_{QRS})$ and $\widehat{\vec{\boldsymbol{u}}}_{T} = (\hat{x}_{T}, \hat{y}_{T}, \hat{z}_{T})$. The regression network consists of two dense hidden layers, each followed by layer normalization and activation with Leaky ReLU, and a dense output layer with six neurons. Since ECGs can exhibit sex- and age-related dissimilarities in morphology [29] that can affect the QRS-T angle [30,31], metadata about sex (*0* for males, or *1* for females) and age (scaled from 0.0 to 1.0) are concatenated into the regression model. Providing hints at the model about a possible association between ECGs and metadata may be valuable when the available spatial information in the input leads is reduced.

3.2. Loss Function

Since the ultimate goal is to determine the QRS-T angle, the most instinctual approach would be to train the model to estimate the VCG-derived α directly instead of $\vec{\boldsymbol{u}}_{QRS}$ and $\vec{\boldsymbol{u}}_{T}$, optimizing it with the mean absolute error (ϵ) loss between α and estimated $\widehat{\alpha}$:

$$\mathcal{L}_{\epsilon}(\alpha, \widehat{\alpha}) = \frac{1}{n}\sum_{i=1}^{n}(|\alpha_i - \widehat{\alpha}_i|), \text{ where } 0° \leq \mathcal{L}_{\epsilon} \leq 180°, \tag{10}$$

and n is the batch size. Direct estimation of the QRS-T angle, albeit intuitive and straightforward, overlooks crucial information about the spatial orientation and position of the QRS and T loops, trivializing the problem of QRS-T angle estimation as explained in Section 2. In sets of reduced-lead ECGs that only carry fragments of all spatial information contained in the VCG, this approach can produce errors in ECGs with visible differences in morphology but similar QRS-T angles. Morphologically different ECGs with QRS-T angles of equivalent range can occur in patients in which the electrical activity of the heart is not conducted in the same direction, that is, the cardiac conduction axis is nonidentical. In two distinct cardiac conduction axes, $\vec{\boldsymbol{u}}_{QRS}$ and $\vec{\boldsymbol{u}}_{T}$ are located in different planes (octants) in the 3D space, but the angle between can still be alike (see Figure X – Missing). To address these scenarios, we devise the model to locate the coordinates of $\vec{\boldsymbol{u}}_{QRS}$ and $\vec{\boldsymbol{u}}_{T}$ instead of α directly, allowing the model to harness any spatial information available in the input leads. The model is guided throughout the 3D space using the Euclidean distance as the parameter to be minimized in the backpropagation algorithm. The 3D Euclidean distance (d_{L2}) between the coordinates of $\vec{\boldsymbol{u}}$ and $\widehat{\vec{\boldsymbol{u}}}$ is computed as:

$$\mathcal{L}_{d_{L2}}(\vec{\boldsymbol{u}}, \widehat{\vec{\boldsymbol{u}}}) = \frac{1}{n}\sum_{i=1}^{n}\sqrt{(x_i - \widehat{x}_i)^2 + (y_i - \widehat{y}_i)^2 + (z_i - \widehat{z}_i)^2}, \tag{11}$$

where, $0 \leq \mathcal{L}_{d_{L2}} \leq 2$ if both $\vec{\boldsymbol{u}}$ and $\widehat{\vec{\boldsymbol{u}}}$ have a magnitude of 1[1]. In order for $\widehat{\alpha}$ to be equal to α, only the direction, but not the magnitude, of the estimated $\widehat{\vec{\boldsymbol{u}}}$ has to match the target $\vec{\boldsymbol{u}}$. Given that the Euclidean distance of two vectors also accounts for differences in magnitude, which is undesirable in this case, we transform $\vec{\boldsymbol{u}}$ and $\widehat{\vec{\boldsymbol{u}}}$ to unit vectors prior to calculating $\mathcal{L}_{d_{L2}}$. Calculating the Euclidean distance between unit vectors avoids wrongfully calculating a high loss in cases of two vectors with the same direction but discrepant magnitudes, which should be zero in this application. The principle is similar to the *cosine similarity*. However, the Euclidean distance is preferable for this case scenario as it permits to navigate throughout each axis in *xyz* plane, whereas the *cosine similarity* only discerns one axis (in the 2D space, the cosine can distinguish quadrant I from II, or IV from III, but not I from IV nor II from III).

Another problem left to address during the training process is cases in which one of the vectors is less complicated to determine than the other (see Figure X – Missing), i.e., the model properly locates one vector but not the other (e.g., $\mathcal{L}_{d_{L2}}(\vec{\boldsymbol{u}}_{T}, \widehat{\vec{\boldsymbol{u}}}_{T}) \approxeq 0$ and $\mathcal{L}_{d_{L2}}(\vec{\boldsymbol{u}}_{QRS}, \widehat{\vec{\boldsymbol{u}}}_{QRS}) \approxeq 1.2$). Significant errors in estimating one vector will inherently affect the accuracy of the QRS-T angle. Since the angle between $\widehat{\vec{\boldsymbol{u}}}_{QRS}$ and $\widehat{\vec{\boldsymbol{u}}}_{T}$ needs to be equivalent to α, we mitigate such cases by confining the model's search grid to preserve the angle $\widehat{\alpha}$ between $\widehat{\vec{\boldsymbol{u}}}_{QRS}$ and $\widehat{\vec{\boldsymbol{u}}}_{T}$ as close as possible to α. Thus, we define the overall loss as a composite function of (10) and (11):

$$\mathcal{L} = w_1\Big(\mathcal{L}_{d_{L2}}(\vec{\boldsymbol{u}}_{QRS}, \widehat{\vec{\boldsymbol{u}}}_{QRS}) + \mathcal{L}_{d_{L2}}(\vec{\boldsymbol{u}}_{T}, \widehat{\vec{\boldsymbol{u}}}_{T})\Big) + w_2\,\mathcal{L}_{\epsilon}(\alpha, \widehat{\alpha}), \tag{12}$$

[1] Two vectors $\vec{\boldsymbol{a}}$ and $\vec{\boldsymbol{b}}$ of magnitude 1, i.e., unit vectors, with opposite directions (circumscribed by angle of 180°) have an Euclidean distance that is the sum of their magnitudes: $\|\vec{\boldsymbol{a}}\| + \|\vec{\boldsymbol{b}}\| = 1 + 1 = 2$.

where w_1 and w_2 are hyperparameters that weigh the penalization factor of $\mathcal{L}_{d_{L2}}$ and $\mathcal{L}_\epsilon$. The proposed composite loss function safeguards the overall accuracy of the model by avoiding that $\mathcal{L}_{d_{L2}}$ of one vector is substantially higher than $\mathcal{L}_{d_{L2}}$ of the other, with the tradeoff of allowing minor errors in the location of both vectors (i.e., $\mathcal{L}_{d_{L2}} \approxeq 0.1$ instead of $\mathcal{L}_{d_{L2}} \approxeq 0$), as long as the angle $\widehat{\alpha}$ between them is close to α. To equalize the scales of $\mathcal{L}_{d_{L2}}$ and $\mathcal{L}_\epsilon$, $\mathcal{L}_\epsilon\left(\alpha, \widehat{\alpha}\right)$ is estimated in radians rather than degrees.

3.3. Tuning of Hyperparameters

Several experiments are conducted to find the most optimal architecture for each of the tested subsets of leads according to the hyperparameters w_1 and w_2, depth D, and the initial number of kernels k. The hyperparameters are chosen among the following options: $D = \{2, 3, 4, 5\}$, $k = \{8, 16\}$, $w_1 = \{0.5, 0.8, 1.0, 1.2, 1.5\} \wedge w_2 = |1 - w_1|$, and $w_2 = \{0.8, 1.0, 1.2, 1.5\} \wedge w_1 = |1 - w_2|$. The hyperparameters D and k are constrained to the above values due to the following. First, complex CNNs employed for image-based applications are likely an overengineered solution for our problem. Second, smaller CNN architectures enhanced with residual connections and case-specific loss functions have recently matched the performance of deeper and more computationally expensive architectures [32]. Third, lightweight and low-complexity models are preferable for deployment in devices with hardware and computational constraints, such as consumer healthcare devices. Training is performed with a batch size of $n = 8$ at an initial learning rate of 0.001 for 100 epochs. After every 20 epochs, the learning rate is reduced by half.

4. Data

The deep learning model is developed and validated on the *Physionet* [33] *PTB-XL* dataset [24], the current largest publicly available dataset of 12-lead ECG recordings. The *PTB-XL* comprises 21 837 clinical recordings of 10 s long ECGs, upsampled to 500 Hz, from 18 885 patients (48% females) with ages ranging from 0 to 95 years. Information on the diagnosis, form, rhythm, and signal quality is provided for all recordings. As to diagnosis, the ECGs are categorized into five different superclasses: Normal (*NORM*), Myocardial Infarction (*MI*), Conduction Disturbance (*CD*), ST/T change (*STTC*), and Hypertrophy (*HYP*). The superclasses are branched into several subclasses, apart from *NORM*.

4.1. Data Preparation and Labeling

Leads *XYZ* are derived from raw ECGs by applying the Kors regression matrix [11], the mathematical transformation that more accurately reconstructs Frank's VCG from an ECG [12], to leads *I*, *II*, and *V1–V6*. The generated 15-lead signals undergo preprocessing comprised of filtering, signal quality assessment and beat averaging. The target vectors $\vec{\boldsymbol{u}}_{QRS}$ and $\vec{\boldsymbol{u}}_T$ are finally computed from the generated signal-averaged leads *XYZ* (VCG) to label the data. Figure 3 illustrates the data preparation process.

4.1.1. Signal Preprocessing

Filtering. High-frequency noise and baseline wandering are filtered with zero-phase low- and high-pass Butterworth filters with cut-off frequencies of 45 Hz and 0.5 Hz.

Signal quality assessment. The signal quality index (SQI) criteria proposed in [34] is applied to each lead individually to eliminate beats of dissimilar morphology, such as ectopic beats or those corrupted by noise. Recordings with at least one lead that contains more than 50% poor-quality beats within the 10 s ECG are considered unanalyzable and hence discarded. ECGs with discernible rhythm disturbances, such as atrial or ventricular flutter or fibrillation, are also excluded from the analysis given their greater predisposition to PQRST delineation errors that can affect the reliability of $\vec{\boldsymbol{u}}_{QRS}$ and $\vec{\boldsymbol{u}}_T$ [27]. In case of rhythm disturbances like bradycardia, tachycardia or sinus arrhythmia, PQRST delineation can be less problematic when signals are of high-quality; thus, such ECGs are still considered for analysis if 70% of all beats satisfy the SQI criteria.

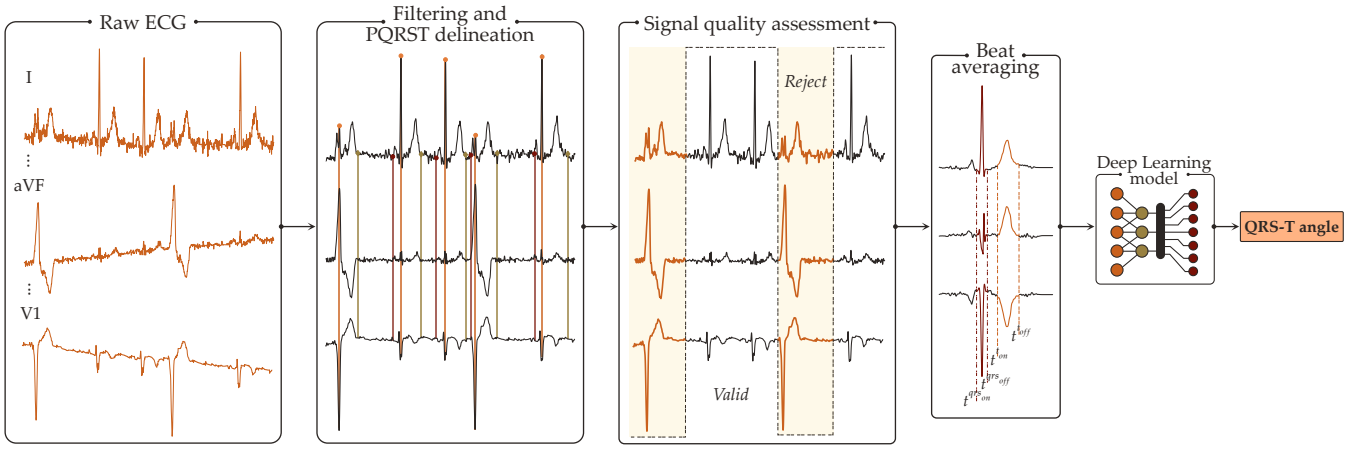

Figure 3. Preprocessing of ECG signals. A signal-average heartbeat representative of each chosen lead is fed to the the proposed deep-learning model for estimating the QRS-T angle. *I need to change this.*

Beat averaging. High-quality beats are aligned using the R-peak as a reference point and averaged, resulting in one signal-averaged heartbeat representative of each chosen input lead. For the purpose of our investigation, we obtain 15 averaged heartbeats.

4.1.2. Data Labeling

Our *training labels*, i.e., the target VCG vectors $\vec{\boldsymbol{u}}_{QRS}$ and $\vec{\boldsymbol{u}}_{T}$ computed from the three averaged beats of leads *XYZ* using the conventional approach described in Section 2 with equations (8), (9). The QRS-T angle is calculated as in (5). The loops onset and offset, t_{QRS_o}, t_{T_o}, t_{QRS_e}, and t_{T_e} are identified with the multilead PQRST delineation algorithm[2] available in the *ECGDeli* [35] toolbox, and adjusted as instructed in [27]. Lastly, the averaged beats are downsampled to 250 Hz and zero-padded to 550 samples to equalize their length. Patient metadata is further added to *training labels*: information about sex is specified as *0* for males and *1* for females, and age is scaled from 0.0 to 1.0.

Of 21 837 clinical recordings, 18 618 are eligible for labeling and analysis. In addition to poor-quality ECGs or with complicated rhythm disturbances, we exclude recordings in which the assigned subclass is underrepresented in the dataset, having less than 100 recordings that meet the described SQI criteria. ECGs of rare subclasses have such unusual morphologies that errors can be introduced into the model due to the scarcity of recordings.

4.2. Exploratory Data Analysis

Exploratory data analysis is performed on the labeled recordings before splitting the data between the training and validation sets. The goal is to eliminate any statistical bias by ensuring that both sets preserve the same distribution of sex, morphological classes, and the spatial QRS-T angle in the ranges of $\alpha = [0{:}5{:}180]^\circ$, as in the original dataset. We center our exploratory data analysis and subsequent splitting around these three attributes due to the following:

- Sex-related morphological differences in the ECG may influence the decision of the regression network (see section 3.1.2); thus, the training set must be proportioned in terms of sex.
- Each of the morphological classes is characterized by distinctive morphological traits. Since contrastive ECG morphologies can still exhibit QRS-T angles of comparable range, the training set must include a diversity of morphologies to prevent the model

[2] Note that robust PQRST delineation algorithms are critical to compute reliable *training labels* for developing the model, but are not necessary in future applications in which only averaged heartbeats and metadata are required as input.

from associating a specific range of QRS-T angles with just one subset of particular morphological traits.

- Randomly splitting the data without considering the uneven distribution of α within specific ranges could result in a disproportionate depiction of specific ranges in the training set, leading to higher errors in other ranges.

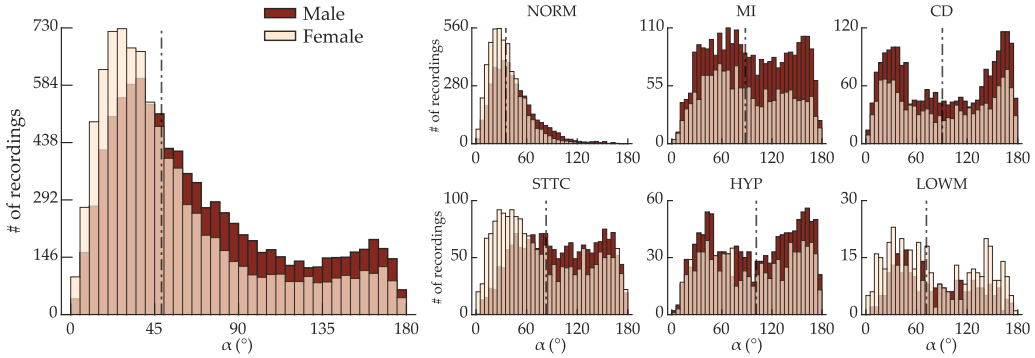

Figure 4. Distribution of spatial QRS-T angles α of across the ranges of $\alpha = [0{:}5{:}180]^\circ$ according to sex for all eligible recordings in the dataset (left) and for each morphological class (right). α is the angle between the the VCG vectors $\vec{\boldsymbol{u}}_{QRS}$ and $\vec{\boldsymbol{u}}_{T}$.

Recordings are divided into six morphological classes: the same five diagnostic superclasses stipulated in the *PTB-XL* dataset, *NORM*, *MI*, *CD*, *STTC*, *HYP*, and low magnitude T waves (*LOWM*). A recording is deemed *LOWM* if the ratio between $\|\vec{\boldsymbol{u}}_T\|$ and $\left\|\vec{\boldsymbol{u}}_{QRS}\right\| < 0.1$. Although signals with low magnitude T waves seem to have a higher propensity to QRS-T angle errors [27] and are often discarded [27,36], we consider to be reasonable to incorporate such signals into this study, given that low magnitude T waves are found routinely in clinical practice.

Figure 4 shows the distribution of α across the ranges of $\alpha = [0{:}5{:}180]^\circ$, according to sex and morphological class. The dataset has a median of 52.9° (interquartile range of 63.3°). The distribution of α, albeit balanced between males and females, varies considerably for each morphological class. Although spatial QRS-T angles $15^\circ \leq \alpha \leq 90^\circ$ comprise the vast majority of the eligible recordings, all other ranges of α are represented by at least 120 recordings, which may be sufficient for deep-learning-based estimation of QRS-T angle with an acceptable error.

4.3. Training and Validation Sets

The data is split separately for females and males in each morphological class to ensure an appropriate data allocation between the training and validation sets. The split is performed as follows. For any given morphological class, 80% female ECGs and 80% of male ECGs with $\alpha = [i{:}i+5[$, for every $i = [0{:}5{:}175]^\circ$, are randomly assigned to the training set. Given the propensity of *LOWM* signals to display larger errors of α, the 50:50 partition ratio is used for this class instead of 80:20. A smaller partition of the *LOWM* class still enables the class to be adequately represented in the training set without excessively misleading the deep learning model. Figure 5 shows that both the training and validation sets preserve the original distribution of α.

5. Experiments and Performance Evaluation

The model is written in Python (v3.8.10) using the Keras abstraction layer on Tensorflow 2.8.0 backend. Model training and testing are performed on a desktop with Windows 10 environment with the following parameters: Intel® Core™ i7-8700k 3.70 GHz CPU with six cores (12-threads), 32 GB of RAM, and NVIDIA® GeForce® GTX 1080Ti.

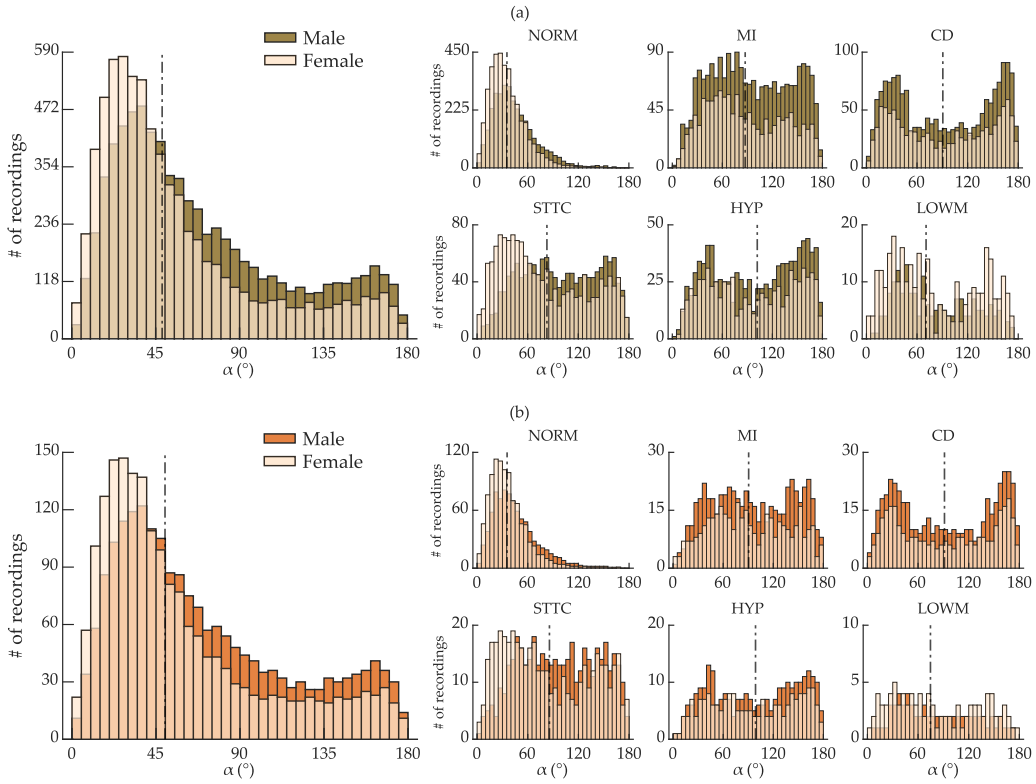

Figure 5. Distribution of spatial QRS-T angle α across the ranges of $\alpha = [0{:}5{:}180]^\circ$ according to sex for all recordings suitable for analysis (left) and for each morphological class (right) in the **(a)** training and **(b)** validation sets.

5.1. Selection of Subsets of ECG Leads

We investigate the performance of our model to estimate the spatial QRS-T angle from various subsets of ECGs leads. The goal is to identify how many leads suffice to estimate the QRS-T angle with acceptable accuracy without sacrificing patient comfortability. We start by configuring the baseline architecture of our model using the leads that contain all the 3D spatial information,XYZ, from which the target $\vec{\boldsymbol{u}}_{QRS}$ and $\vec{\boldsymbol{u}}_{T}$ are derived. Next, we progressively trim the number of precordial leads that carry insights about the spatial position of $\vec{\boldsymbol{u}}_{QRS}$ and $\vec{\boldsymbol{u}}_{T}$ in each of the X, Y, and Z axes. The baseline model architecture is optimized for sets of reduced-lead ECGs that incorporate a minimum of one lead shown to reflect each orthogonal axis: $X \subseteq \{I, V5, V6\}$; $Y \subseteq \{II, III, aVF\}$; and $Z \subseteq \{V1, V2, V3\}$ [13].

Since this research ultimately aims to develop a method to facilitate QRS-T angle monitoring in free-living conditions, we only test sets of reduced-lead ECGs that can be acquired from commercialized consumer healthcare devices. Registration of frontal leads is straightforward: all six frontal leads ($I, II, III, aVL, aVR, aVF$) can be derived from any device with two-frontal channels. However, most consumer healthcare devices equipped for frontal and precordial lead registration offer no more than two precordial leads: $V2$ and $V6$. Thus, we limit our experiments to subsets of leads $\{I, II, III, aVL, aVR, aVF, V2, V6\}$.

While a decline in performance is anticipated as the number of precordial leads decreases, we also explore as a proof-of-concept the ability of our model to estimate the spatial QRS-T angle from subsets of exclusively frontal leads. In this article, we only present the results of the best subset of leads: first XYZ, then few-frontal-and-two-precordial leads, few-frontal-and-one-precordial leads, and lastly, exclusively frontal leads.

5.2. Performance Metrics

I need to write this with proper equations.

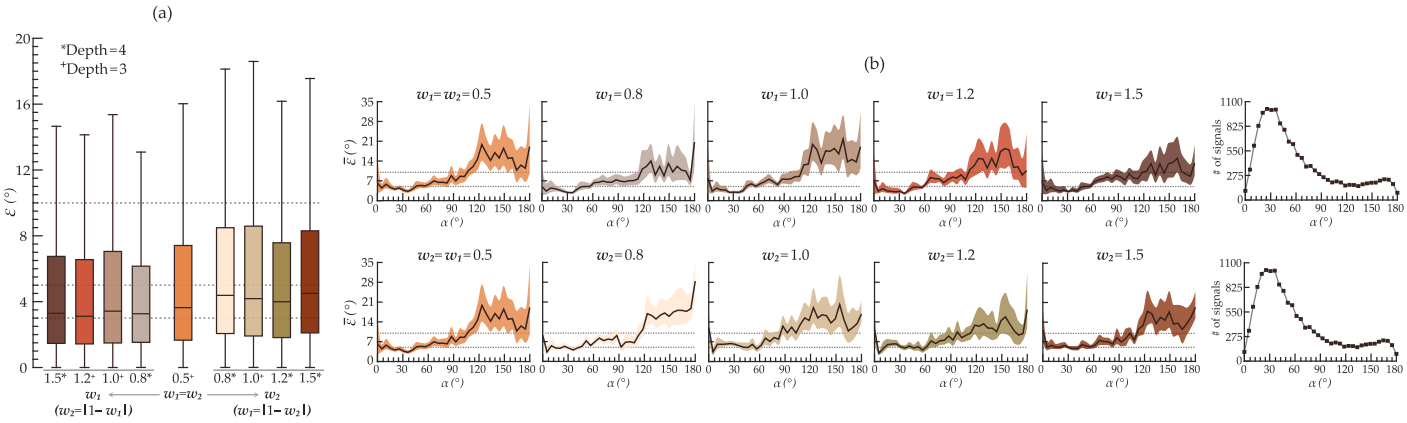

Figure 6. Performance comparison of the best deep learning model configuration trained with various combinations of hyperparameters w_1 and w_2 to predict the spatial QRS-T angle from leads XYZ. (a) Boxplot of absolute error ϵ obtained in the validation dataset (outliers not shown) using a model trained at different values of w_1 and w_2. w_1 increases in the left side, wheres w_2 in the right. The other hyperparameter value is obtained as $|1 - w|$ on each side. (b) Mean absolute error $\bar{\epsilon}$ across the ranges of α=[0:5:180]° for increasing w_1 (top row) and w_2 (bottom row). The upper and lower boundaries represent the 95% confidence interval of $\bar{\epsilon}$. The last column displays the total number of recordings in the training dataset for each range of α.

To make the results more intuitive to interpret, we evaluate the model's performance as:

- Residuals between the predicted $\widehat{\alpha}$ and α: $\widehat{\alpha} - \alpha$. Bland-Altman plots are used for this effect. The following statistics are computed: bias, limits of agreement, coefficient of variation (CV), and reproducibility coefficient (RPC) calculated using nonparametric methods.
- The root square error ϵ: $\epsilon = \sqrt{(\widehat{\alpha}_i - \alpha_i)^2}$. Scatter plots, boxplots and line plots showing the ϵ and the mean confidence intervals (CI) at 95%. The values of mean, median, standard deviation, and CI are calculated using bootstrap as the data does not follow a normal distribution.

6. Results

6.1. Influence of Different Hyperparameters on the Performance of the Model

Figure 6 displays the performance of the proposed deep learning model to estimate the spatial QRS-T angle α from leads XYZ when trained with various combinations of hyperparameters w_1 and w_2. Only the depth at which the lowest median error $\tilde{\epsilon}$ was obtained is shown for each combination. An initial number of kernels $k = 8$ was found to be sufficient to train the model for leads XYZ as the input leads. As hypothesized, prioritizing the Euclidean distance $E(\vec{\boldsymbol{u}}, \widehat{\vec{\boldsymbol{u}}})$ over the angle $S(\alpha, \widehat{\alpha})$ as the predominant penalization factor, that is, $w_1 > w_2$, results in smaller errors. However, the differences are not substantial in the ranges of α represented by at least 250 recordings in the training dataset ($\alpha < 90°$). Combining the Euclidean distance (w_1) and the angle (w_2) in the loss function yields better results than using each metric alone ([w_1=1.0, w_2=0.0] and vice versa). Although the lowest $\tilde{\epsilon}$ was reached with [w_1=1.2, w_2=0.2] at D=3 ($\tilde{\epsilon}$=3.1°), the model trained with [w_1=0.8, w_2=0.2] at D=4 ($\tilde{\epsilon}$=3.3°) achieved the narrowest interquartile range (4.6° vs. 5.1°) and the best overall results throughout all ranges of α. In particular, this configuration outperformed the others for $\alpha \geq 90°$, showing lower absolute mean errors $\bar{\epsilon}$ despite the smaller number of recordings in the training dataset for such ranges.

For all investigated sets of reduced-lead ECGs given as input leads, we verified that the model trained with the same hyperparameters [w_1=0.8, w_2=0.2], but with D=3 and k=16 achieved the lowest errors in estimating the spatial QRS-T angle. Contrastively to

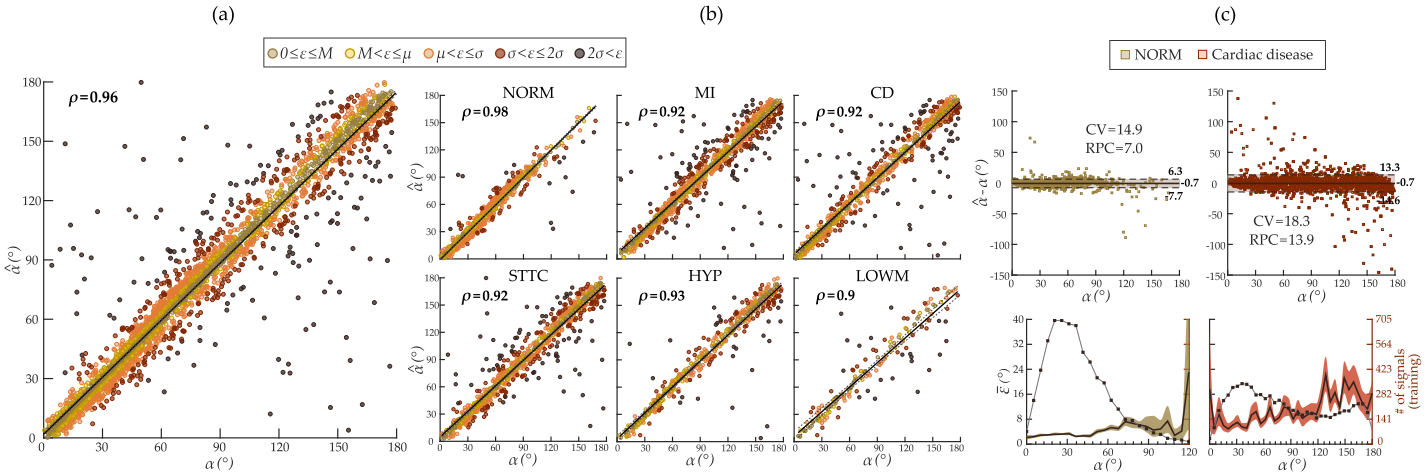

Figure 7. Analysis of the estimated spatial QRS-T angle $\hat{\alpha}$ from leads *XYZ* using a model trained with $[w_1=0.8, w_2=0.2]$ and $k=8$ at $D=4$. Scatter plot diagrams for (**a**) all signals and (**b**) each of the six classes in the validation dataset. Different colors group the absolute error ϵ of each $\hat{\alpha}$ according to the absolute median ($\tilde{\epsilon}$), mean ($\bar{\epsilon}$), and standard deviation (σ_ϵ) error. (**c**) Bland-Altman plot (top row) and variation of $\bar{\epsilon}$ (bottom row) across the ranges of α=[0:5:180]° for signals with normal (NORM) and diseased cardiac function. The upper and lower boundaries show the 95% confidence interval of $\bar{\epsilon}$. The right axis indicates the number of recordings used in training for each respective range of α[3].

leads XYZ, combinations of hyperparamaters in which $w_2 > w_1$ produced substantially higher errors than in those with $w_1 > w_2$, indicating that the adoption of metrics that guide the deep learning model in the 3D space is a favored choice. Concatenation of patient metadata (sex and age) into the feature map slightly improves the estimation of the QRS-T angle in sets of reduced-lead ECGs. However, its impact is negligible if leads XYZ are given as input leads. Table X discloses more details about the training hyperparameters, including batch size and learning rate, and results on the training dataset.

6.2. Estimation of spatial QRS-T Angle

Figures 7–10 show in detail the performance of the best configuration model to estimate the spatial QRS-T angle using *XYZ* leads (Figure 7) and various sets of reduced-lead ECGs: *I-aVF-V2-V6* (Figure 8), *I-II-aVF-V2* (Figure 9), and frontal leads *I-II-aVL-aVF* (Figure 10). Table 1 discloses the obtained root-mean-square-error (RMSE), mean ($\bar{\epsilon}$) and median ($\tilde{\epsilon}$) absolute error for each set of leads in the validation dataset. TODO: Add table footnotes explaining the ranges of Alpha and the metrics The lowest errors are naturally seen in

Table 1. Performance of the proposed deep learning model to estimate the spatial QRS-T angle in the validation dataset.

Class	Range of α	Performance metric											
		RMSE (°)				$\bar{\epsilon}$ (°)				$\tilde{\epsilon}$ (°)			
		XYZ	*I-aVF-V2-V6*	*I-II-aVF-V2*	*I-II-aVL-aVF*	*XYZ*	*I-aVF-V2-V6*	*I-II-aVF-V2*	*I-II-aVL-aVF*	*XYZ*	*I-aVF-V2-V6*	*I-II-aVF-V2*	*I-II-aVL-aVF*
All val. data	0° ≤ α ≤ 180°	12.2	17.2	18.4	25.4	5.8	10.3	11.4	17.9	3.3	6.4	7.3	12.7
NORM	15° ≤ α ≤ 180°	6.3	13.8	14.4	20.7	3.5	8.6	9.3	14.4	2.6	5.8	6.4	10.2
	5° ≤ α ≤ 70°	4.6	11.0	11.1	15.2	3.0	7.2	7.6	11.7	2.4	5.1	5.7	9.8
Cardiac disease	15° ≤ α ≤ 180°	16.4	19.9	21.3	28.5	8.6	12.1	13.6	20.3	4.9	7.4	8.8	13.9

leads *XYZ* since they are the ones from which the reference $\vec{u}_{QRS}$, $\vec{u}_T$, and α are derived. With the downsizing of precordial leads given as input, the available spatial information is reduced, challenging the model's ability to estimate the spatial QRS-T angle. In the whole validation dataset, the correlation between $\hat{\alpha}$ and α, albeit strong, decreases from $\rho=0.96$ for

[3] Since the number of NORM subjects with α >120° is almost negligible, $\bar{\epsilon}$ is not shown for these ranges of α.

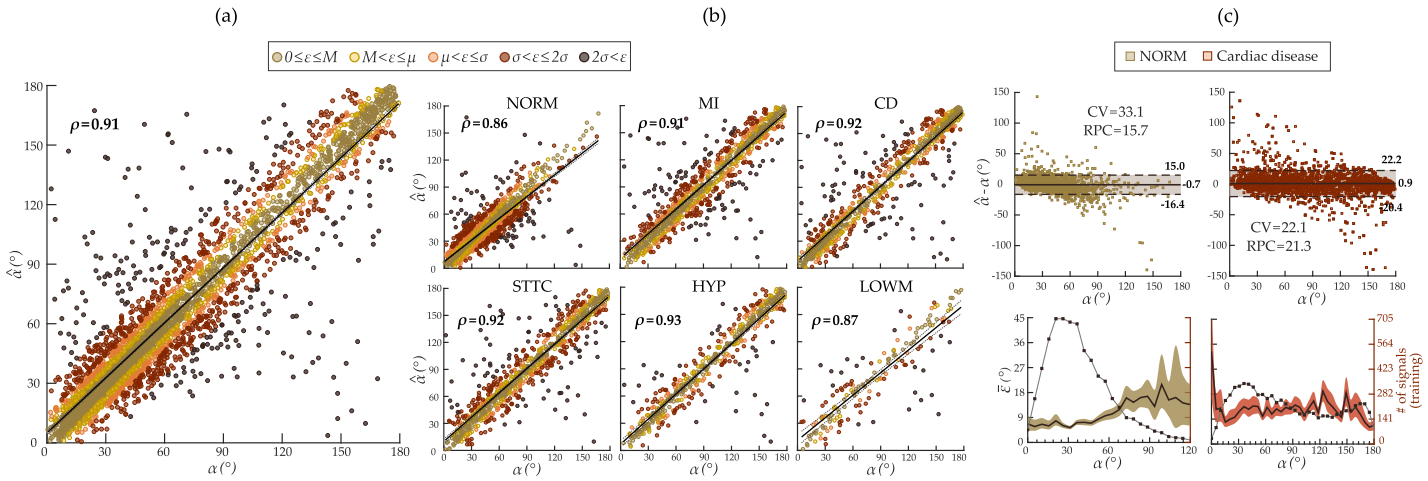

Figure 8. Analysis of the estimated spatial QRS-T angle $\hat{\alpha}$ from leads *I-aVF-V2-V6* using a model trained with $[w_1 = 0.8, w_2 = 0.2]$ and $k = 16$ at $D = 3$. Scatter plot diagrams for (**a**) all signals and (**b**) each of the six classes in the validation dataset. Different colors group the absolute error ϵ of each $\hat{\alpha}$ according to the absolute median ($\tilde{\epsilon}$), mean ($\bar{\epsilon}$), and standard deviation (σ_ϵ) error. (**c**) Bland-Altman plot (top row) and variation of $\bar{\epsilon}$ (bottom row) across the ranges of α=[0:5:180]° for signals with normal (NORM) and diseased cardiac function. The upper and lower boundaries show the 95% confidence interval of $\bar{\epsilon}$. The right axis indicates the number of recordings used in training for each respective range of α[3].

XYZ leads to $\rho = 0.91$ for leads *I-aVF-V2-V6* (two precordial), $\rho = 0.90$ for *I-II-aVF-V2* (one precordial), and $\rho = 0.77$ for *I-II-aVL-aVF* (solely frontal).

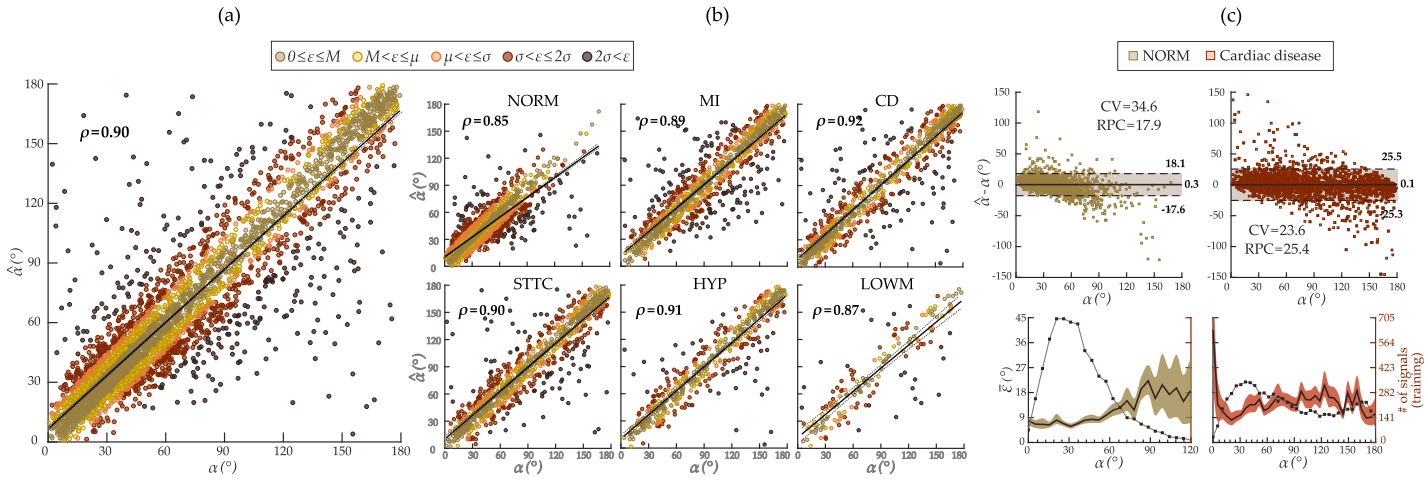

Figure 9. Analysis of the estimated spatial QRS-T angle $\hat{\alpha}$ from leads *I-II-aVF-V2* using a model trained with $[w_1 = 0.8, w_2 = 0.2]$ and $k = 16$ at $D = 3$. Scatter plot diagrams for (**a**) all signals and (**b**) each of the six classes in the validation dataset. Different colors group the absolute error ϵ of each $\hat{\alpha}$ according to the absolute median ($\tilde{\epsilon}$), mean ($\bar{\epsilon}$), and standard deviation (σ_ϵ) error. (**c**) Bland-Altman plot (top row) and variation of $\bar{\epsilon}$ (bottom row) across the ranges of α=[0:5:180]° for signals with normal (NORM) and diseased cardiac function. The upper and lower boundaries show the 95% confidence interval of $\bar{\epsilon}$. The right axis indicates the number of recordings used in training for each respective range of α[3].

In signals with cardiac disease (classes CD, MI, HYP, STTC, and LOWM), the correlation between $\hat{\alpha}$ and α in sets of ECGs with at least one precordial lead is rather similar to that of *XYZ* leads, with ρ being slightly below 0.9 in MI and LOWM in *I-II-aVF-V2*, and $\rho \geq 0.90$ in other classes. In the set of solely frontal leads (*I-II-aVL-aVF*), $\rho = 0.75$ for LOWM

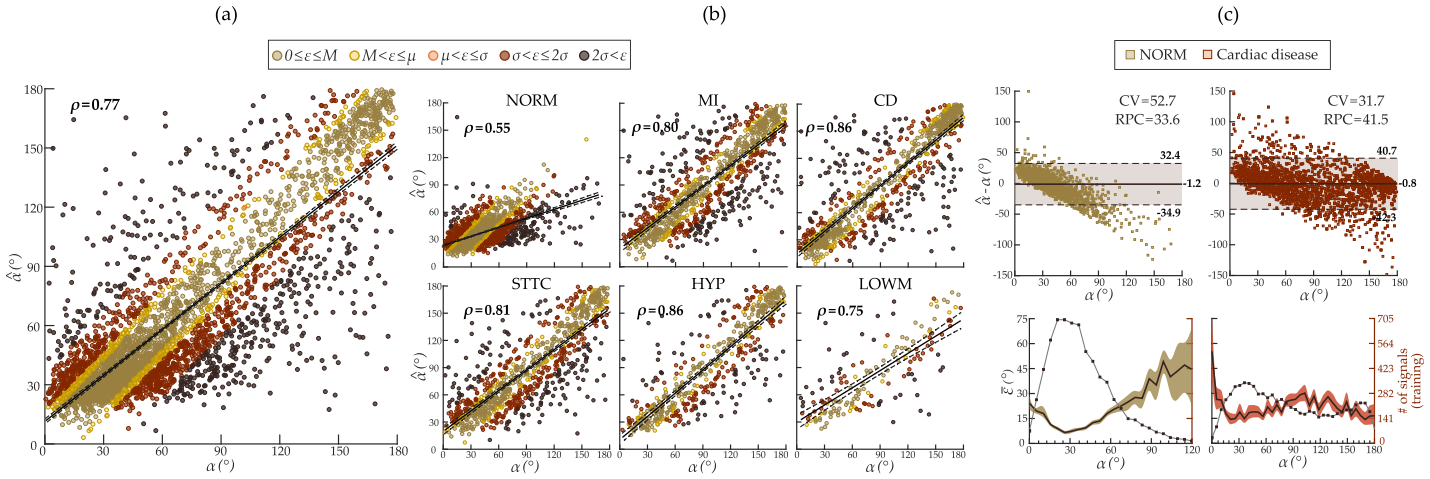

Figure 10. Analysis of the estimated spatial QRS-T angle $\hat{\alpha}$ from frontal leads *I-II-aVL-aVF* using a model trained with [w_1=0.8, w_2=0.2] and k=16 at D=3. Scatter plot diagrams for (**a**) all signals and (**b**) each of the six classes in the validation dataset. Different colors group the absolute error ϵ of each $\hat{\alpha}$ according to the absolute median ($\tilde{\epsilon}$), mean ($\bar{\epsilon}$), and standard deviation (σ_ϵ) error. (**c**) Bland-Altman plot (top row) and variation of $\bar{\epsilon}$ (bottom row) across the ranges of α=[0:5:180]° for signals with normal (NORM) and diseased cardiac function. The upper and lower boundaries show the 95% confidence interval of $\bar{\epsilon}$. The right axis indicates the number of recordings used in training for each respective range of α[3].

and $\rho \geq 0.80$ for the other four classes. With the reduction of spatial information, RMSE, $\bar{\epsilon}$ and $\tilde{\epsilon}$ increase nonetheless (see Table 1. In leads *XYZ*, the model exhibited markedly higher $\bar{\epsilon}$ in ranges of α that are represented by less than 150 recordings with cardiac disease in the training dataset (α<15° and $\alpha \geq$ 115°). Interestingly, the model did not show the same sensitivity to the number of recordings in sets of reduced-lead ECGs. Although $\bar{\epsilon}$ is higher in reduced-lead ECGs than in *XYZ* leads, $\bar{\epsilon}$ increases only by a small margin for $\alpha \geq$ 115° in comparison to 15° $\leq \alpha <$ 115°.

Estimating the spatial QRS-T angle appeared to be unexpectedly more complicated in normal (NORM) recordings than in those with cardiac diseases for any set of reduced-lead ECGs, but not for leads *XYZ*. While the performance metrics of NORM signals are lower than those of cardiac disease in ranges of α that are vastly more represented in the training dataset (5° $\leq \alpha <$ 70° for NORM signals), the agreement between $\hat{\alpha}$ and α is smaller than in any other class: ρ= 0.86 for *I-aVF-V2-V6*, ρ= 0.85 for *I-II-aVF-V2*, and even smaller for *I-II-aVL-aVF* with ρ= 0.55, whereas ρ= 0.98 for leads *XYZ*. Just as in ECGs with cardiac diseases, RMSE, $\bar{\epsilon}$ and $\tilde{\epsilon}$ increase as the amount of spatial information in the input leads diminishes for NORM recordings. Even so, for range of 5° $\leq \alpha <$ 70°, $\bar{\epsilon}$=3.0° for *XYZ*, $\bar{\epsilon}$=7.2° for *I-II-V2-V6*, $\bar{\epsilon}$=7.6° for *I-II-aVL-V2*, and $\bar{\epsilon}$=11.7° for *I-II-aVL-aVF*.

Bland-Altman plots in Figures 7c–10c corroborate the abovementioned results. The limits of agreement between $\hat{\alpha} - \alpha$ and α are narrower in leads *XYZ* and start to broaden as the number of precordial leads decreases, with recordings of class NORM having less variability from the median bias than those with cardiac disease. In leads *I-II-aVL-aVF*, however, the model appears to be moderately biased, but still homoscedastic, i.e., the variance across different ranges of α is similar. Such a pattern is characteristic when a latent variable has not been fully enclosed in the model; in this case, the sagittal and transverse components supplied by the z coordinate.

Figure 7 displays the distribution of the Euclidean distance $E(\vec{\boldsymbol{u}}, \hat{\vec{\boldsymbol{u}}})$ between $\vec{\boldsymbol{u}}_{QRS}$ and $\hat{\vec{\boldsymbol{u}}}_{QRS}$, and $\vec{\boldsymbol{u}}_T$ and $\hat{\vec{\boldsymbol{u}}}_T$ in each of the three planes: xy (frontal), xz (transverse), and yz (sagittal). The distance is calculated as the projection of $\vec{\boldsymbol{u}}$ and $\hat{\vec{\boldsymbol{u}}}$ in each respective plane. $E(\vec{\boldsymbol{u}}, \hat{\vec{\boldsymbol{u}}})$ gradually lengthens in every plane from leads *XYZ* to *I-aVF-V2-V6* and *I-II-aVF-V2* but becomes discernibly higher in the xz and yz planes in frontal leads *I-II-aVL-aVF*, which

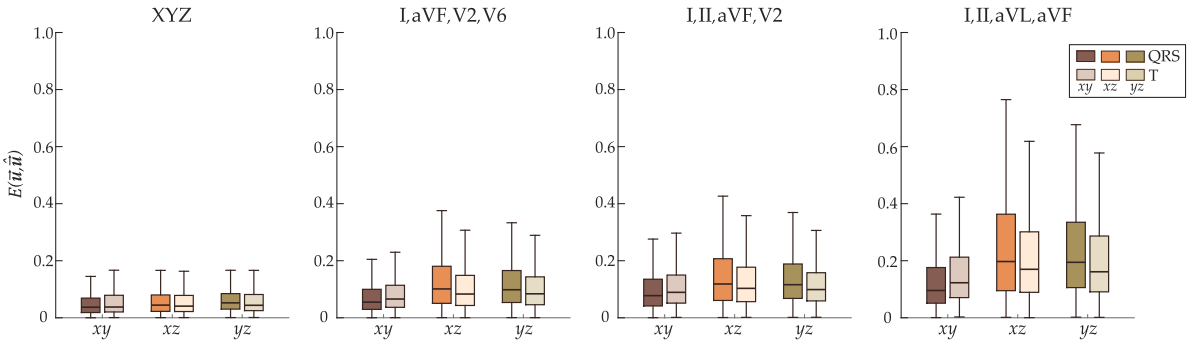

Figure 11. Distribution of the Euclidean distance $E(\vec{u},\hat{\vec{u}})$ between $\vec{u}_{QRS}$ and $\hat{\vec{u}}_{QRS}$, and $\vec{u}_T$ and $\hat{\vec{u}}_T$ in each of the three planes: xy (frontal), xz (transverse), and yz (sagittal).

only carry information in the xy plane. Larger $E(\vec{u},\hat{\vec{u}})$ suggests the model encountered extra obstacles to estimate the vector's coordinates within the specified plane.

7. Discussion

[1. Significance of our work]

Monitoring the spatial QRS-T angle, evidenced as one of the most propitious markers for risk assessment of SCD [7,8], was presumed to be impracticable in out-of-hospital settings thus far. Our research introduces a deep-learning-based method to measure the spatial QRS-T angle using a set of reduced-lead ECGs that can conveniently be recorded with consumer healthcare devices. Our proposed model, albeit prototypal, sparks scientific interest in engineering methods for out-of-hospital monitoring of the QRS-T angle, which can lead to substantial contributions toward harnessing the diagnostic value of the QRS-T angle for cardiovascular health assessment in free-living conditions. To the best of our knowledge, this is the first study to examine whether it is conceivable to estimate the QRS-T angle using reduced-lead ECGs.

[2. Possible Application in ambulatory monitoring]

One attractive attribute of the proposed deep learning model is its simplicity. When looking at the computational demands of the whole algorithm, the QRS-T angle can be estimated in almost real-time, with the preprocessing stage exercising more computational time and resources than the deep learning model itself. In recordings scenarios that assure that 10-to-15 s long ECGs are registered with sufficient quality to warrant low-complexity filtering in the preprocessing stage, the spatial QRS-T angle can be calculated in a few seconds with the advantage of not needing PQRST delineation. In ambulatory recordings, PQRST delineation is often problematic due to noise. Even if the conventional methods for QRS-T angle estimation could be applied to reduced-lead ECGs, such methods demand unequivocally precise PQRST delineation algorithms. Since even minor inaccuracies in PQRST delineation can result in sizeable QRS-T angle errors [27], the conventional methods would be unpropitious for ambulatory applications.

Our model measured the spatial QRS-T angle with reasonable accuracy from a set of three frontal-and-one precordial leads, *I*, *II*, *aVF*, *V2*, that can be registered with three electrodes instead of the eight required to derive the QRS-T angle using the conventional approach. Requiring one precordial lead evidently restricts the type of consumer healthcare devices suitable for deploying our deep learning model, precluding the use of devices that maximize comfort, such as wrist-worn wearables [37], which only register frontal-lead ECGs. Nevertheless, the market already offers a handful of practical devices that acquire frontal-and-one precordial lead ECGs with an acceptable degree of comfortableness [38], namely those patch-based (e.g., Bittium OmegaSnap™ [39]) or contact-based textile (e.g., Viscero ECG vest [40]) ECG electrodes. A downsize of eight to three electrodes is still a substantive improvement. Even if the comfort level of three electrodes is lower than that of other wearables, the existing patch- or textile-based ECG devices are durable, easy to

configure, and may be adequate for intermittent monitoring of the QRS-T angle in out-of-hospital settings. Recent advancements in the reconstruction of the standard 12-lead ECG from sets of reduced-lead ECGs have, however, demonstrated to be possible to derive lead *V2* from lead *II* [41] in healthy subjects. The encouraging preliminary results indicate a prospective solution for estimating the QRS-T angle with comfortable wearable devices in the future.

[3. Considerations about the baseline architecture of the model]

The baseline architecture of our model is engineered to be accurate yet simple enough to be lightweight and have the low computational power to be integrated into consumer healthcare devices. Compared to other CNN1Ds for ECG analysis, often comprised of 8-to-34 [18,21,42,43] blocks of layers, our baseline architecture of three-to-four blocks ($D = \{3, 4\}$) and $k = 16$ suffices to get satisfactory results. While popular due to their high accuracy, deeper neural networks also entail larger training datasets and computational resources that can hamper the deployment of the network in devices such as wearables. Adopting deeper neural networks does not necessarily translate into significant improvements in accuracy to justify the tradeoffs in resources if the goal application is for out-of-hospital monitoring of QRS-T angle.

Smaller networks like ours, or as in the one applied for automatic diagnosis of 12-lead ECGs [42], have been reported to match the performance of their deeper counterparts when enhanced with custom blocks such as residual connections, squeeze-and-excitation, atrous spatial pooling, or case-specific loss functions [32]. Our strategy involved residual blocks with a predominant focus on a personalized loss function. Our proposed loss function combines two metrics, each with their penalization weight, to optimize the model in the backpropagation algorithm: the Euclidean distance (w_1) and the QRS-T angle (w_2). Prioritizing the Euclidean distance over the QRS-T angle (i.e., $w_1 > w_2$) as the main penalization factor in the loss function results in smaller errors, namely in sets of reduced-leads ECGs. Optimization with the Euclidean distance combined with the QRS-T angle instead of the QRS-T angle alone allows the model to recognize that ECGs with visible differences in morphology can still have similar QRS-T angles, minimizing the chances of the model associating a distinct morphology to a particular range of QRS-T angles. Morphologically different ECGs with similar QRS-T angles are often the case in patients with distinctive cardiac conduction axes in which the direction of the overall electrical activity of the heart is not the same. In a 3D space, this means that the vectors $\vec{\boldsymbol{u}}_{QRS}$ and $\vec{\boldsymbol{u}}_{T}$ are located in different planes (octants), but the angle between them does not necessarily differ. Searching for the coordinates of both target vectors helps the model leverage any available information to boost accuracy. Thus, adopting metrics that guide the model in the 3D space is a favorable choice.

[4. Training errors]

List of points to mention:

- Errors increase as the spatial information decreases;
- The largest errors are seen in ranges of α that have less recordings;
- Why the class Norm shows more errors
- What is the acceptable error in a clinical point of view?

[5. Frontal lead estimation] List of points to mention:

- Proof of concept: where it works and where it fails;
- Hierarchical classification and then regression might be suitable

[6. Limitations]

7.1. Rationale Behind Dataset Selection

Although datasets that include XYZ lead signals registered synchronously with 12-lead ECGs would be ideal for estimating $\vec{\boldsymbol{u}}_{QRS}$ and $\vec{\boldsymbol{u}}_{T}$, we consider the two existing datasets, PTB [44] and CSE [45], inadequate for designing a deep learning model on the following grounds. First, the CSE dataset has restricted access. Second, even with data

augmentation, the total number of recordings combined from these two datasets would still be considerably smaller than that of the PTB-XL. Third, the PTB and CSE datasets are unbalanced in terms of sex, age, and lack diversity in both cardiac diseases and healthy controls. In contrast, the PTB-XL dataset provides a realistic representation of the human population, covering a wide spectrum of diseases, comorbidities, and healthy controls. Thus, due to its size, availability, and diversity, the PTB-XL dataset is preferable for the development and evaluation of deep learning models.

8. Conclusions

A deep learning neural network- based estimator of the spatial QRS-T angle from a reduced number of ECG leads is proposed and investigated. Training of the algorithm is supported with the innovative loss function adapted to the application. A gradual reduction of ECG leads from a publicly available dataset of clinical ECG recordings was used for training, validation, and testing. The results suggest that machine learning-based estimation of spatial QRS-T angle from a few frontal and at least one precordial leads is possible with the accuracy sufficient for detection of abnormal QRS-T angles. A good compromise between the error and a comfortability was achieved by using the following ECG leads: I, II, aVF, V2. The study demonstrates that the proposed approach could be of value for a prolonged ambulatory monitoring of patients using wearable patch electrodes with miniature ECG devices. Chronic patients with cardiac and kidney disease could potentially benefit from this technology.

Even though the estimation errors naturally increase with the reduction of spatial information available in the input leads, the results indicate that reduced-lead estimation of the QRS-T angle is indeed achievable.

Methods that facilitate out-of-hospital monitoring of spatial QRS-T angle, such as our proposed model, spark scientific interest and novelty. Further engineering and refinement of such methods can lead to substantial contributions toward harnessing the diagnostic value of the QRS-T angle for cardiovascular health assessment in free-living conditions.

Author Contributions: Conceptualization and software, A.S.R. and R.A.; methodology, data curation, investigation, formal analysis, visualization, and writing–original draft, A.S.R.; formal analysis and writing–review & editing, M.L., P.L. and V.M.; funding acquisition, V.M. All authors have read and agreed to the submitted version of the manuscript.

Funding: This work was supported by the European Regional Development Fund with the Research Council of Lithuania (LMTLT) under Project 01.2.2-LMT-K-718-01-0030.

Conflicts of Interest: The authors declare no conflicts of interest.

Abbreviations

The following abbreviations are used in this manuscript:

CNN	Convolutional neural network
CNN1D	1D convolutional neural network
SCD	Sudden Cardiac Death
ECG	Electrocardiogram
VCG	Vectocardiogram
TCRT	Total cosine R to T
PTB-XL	A large publicly available electrocardiography dataset
NORM	Normal
CD	Conduction Disturbance
MI	Myocardial Infarction
HYP	Hypertrophy
STTC	Change in ST-T segment
LOWM	Low magnitude (i.e. flat) T waves

References

1. Waks, J.W.; Sitlani, C.M.; Soliman, E.Z.; Kabir, M.; Ghafoori, E.; Biggs, M.L.; Henrikson, C.A.; Sotoodehnia, N.; Biering-Sørensen, T.; Agarwal, S.K.; et al. Global Electric Heterogeneity Risk Score for Prediction of Sudden Cardiac Death in the General Population. *Circulation* **2016**, *133*, 2222–2234. doi:10.1161/circulationaha.116.021306.
2. Hayashi, M.; Shimizu, W.; Albert, C.M. The Spectrum of Epidemiology Underlying Sudden Cardiac Death. *Circulation Research* **2015**, *116*, 1887–1906. doi:10.1161/circresaha.116.304521.
3. Srinivasan, N.T.; Schilling, R.J.; and. Sudden Cardiac Death and Arrhythmias. *Arrhythmia &amp Electrophysiology Review* **2018**, *7*, 111. doi:10.15420/aer.2018:15:2.
4. Osadchii, O.E. Role of abnormal repolarization in the mechanism of cardiac arrhythmia. *Acta Physiologica* **2017**, *220*, 1–71. doi:10.1111/apha.12902.
5. Haïssaguerre, M.; Derval, N.; Sacher, F.; Jesel, L.; Deisenhofer, I.; de Roy, L.; Pasquié, J.L.; Nogami, A.; Babuty, D.; Yli-Mayry, S.; et al. Sudden Cardiac Arrest Associated with Early Repolarization. *New England Journal of Medicine* **2008**, *358*, 2016–2023. doi:10.1056/nejmoa071968.
6. Kannel, W.B.; Anderson, K.; McGee, D.L.; Degatano, L.S.; Stampfer, M.J. Nonspecific electrocardiographic abnormality as a predictor of coronary heart disease: The Framingham Study. *American Heart Journal* **1987**, *113*, 370–376. doi:10.1016/0002-8703(87)90280-8.
7. Oehler, A.; Feldman, T.; Henrikson, C.A.; Tereshchenko, L.G. QRS-T Angle: A Review. *Annals of Noninvasive Electrocardiology* **2014**, *19*, 534–542. doi:10.1111/anec.12206.
8. Zhang, X.; Zhu, Q.; Zhu, L.; Jiang, H.; Xie, J.; Huang, W.; Xu, B. Spatial/Frontal QRS-T Angle Predicts All-Cause Mortality and Cardiac Mortality: A Meta-Analysis. *PloS one* **2015**, *10*. doi:10.1371/JOURNAL.PONE.0136174.
9. Chua, K.C.; Teodorescu, C.; Reinier, K.; Uy-Evanado, A.; Aro, A.L.; Nair, S.G.; Chugh, H.; Jui, J.; Chugh, S.S. Wide QRS-T Angle on the 12-Lead ECG as a Predictor of Sudden Death Beyond the LV Ejection Fraction. *Journal of cardiovascular electrophysiology* **2016**, *27*, 833–839. doi:10.1111/JCE.12989.
10. Acar, B.; Yi, G.; Hnatkova, K.; Malik, M. Spatial, temporal and wavefront direction characteristics of 12-lead T-wave morphology. *Medical &amp Biological Engineering &amp Computing* **1999**, *37*, 574–584. doi:10.1007/bf02513351.
11. KORS, J.A.; HERPEN, G.V.; SITTIG, A.C.; BEMMEL, J.H.V. Reconstruction of the Frank vectorcardiogram from standard electrocardiographic leads: diagnostic comparison of different methods. *European Heart Journal* **1990**, *11*, 1083–1092. doi:10.1093/oxfordjournals.eurheartj.a059647.
12. Jaros, R.; Martinek, R.; Danys, L. Comparison of Different Electrocardiography with Vectorcardiography Transformations. *Sensors* **2019**, *19*, 3072. doi:10.3390/s19143072.
13. Maheshwari, S.; Acharyya, A.; Schiariti, M.; Puddu, P.E. Frank vectorcardiographic system from standard 12 lead ECG: An effort to enhance cardiovascular diagnosis. *Journal of Electrocardiology* **2016**, *49*, 231–242. doi:10.1016/j.jelectrocard.2015.12.008.
14. Voulgari, C.; Pagoni, S.; Tesfaye, S.; Tentolouris, N. The Spatial QRS-T Angle: Implications in Clinical Practice. *Current Cardiology Reviews* **2013**, *9*, 197–210. doi:10.2174/1573403x113099990031.
15. Poulikakos, D.; Hnatkova, K.; Skampardoni, S.; Green, D.; Kalra, P.; Malik, M. Sudden Cardiac Death in Dialysis: Arrhythmic Mechanisms and the Value of Non-invasive Electrophysiology. *Frontiers in Physiology* **2019**, *10*. doi:10.3389/fphys.2019.00144.
16. Diagnostic utility of the spatial versus individual planar QRS-T angles in cardiac disease detection. *Journal of Electrocardiology* **2011**, *44*, 404–409. doi:10.1016/J.JELECTROCARD.2011.01.001.
17. Zakaria, H.; Hasimun, P. Frontal QRS-T Angle Measurement in Mice. 2019 International Symposium on Electronics and Smart Devices (ISESD), 2019, pp. 1–4. doi:10.1109/ISESD.2019.8909639.
18. Wu, M.; Lu, Y.; Yang, W.; Wong, S.Y. A Study on Arrhythmia via ECG Signal Classification Using the Convolutional Neural Network. *Frontiers in Computational Neuroscience* **2021**, *14*. doi:10.3389/fncom.2020.564015.
19. Hsieh, C.H.; Li, Y.S.; Hwang, B.J.; Hsiao, C.H. Detection of Atrial Fibrillation Using 1D Convolutional Neural Network. *Sensors* **2020**, *20*, 2136. doi:10.3390/s20072136.
20. Bai, Y.; Zhang, L.; Wan, D.; Xie, Y.; Deng, H. Detection of sleep apnea syndrome by CNN based on ECG. *Journal of Physics: Conference Series* **2021**, *1757*, 012043. doi:10.1088/1742-6596/1757/1/012043.
21. Chang, H.Y.; Yeh, C.Y.; Lee, C.T.; Lin, C.C. A Sleep Apnea Detection System Based on a One-Dimensional Deep Convolution Neural Network Model Using Single-Lead Electrocardiogram. *Sensors* **2020**, *20*, 4157. doi:10.3390/s20154157.
22. Grande-Fidalgo, A.; Calpe, J.; Redón, M.; Millán-Navarro, C.; Soria-Olivas, E. Lead Reconstruction Using Artificial Neural Networks for Ambulatory ECG Acquisition. *Sensors (Basel, Switzerland)* **2021**, *21*. doi:10.3390/S21165542.
23. Sohn, J.; Yang, S.; Lee, J.; Ku, Y.; Kim, H.C. Reconstruction of 12-Lead Electrocardiogram from a Three-Lead Patch-Type Device Using a LSTM Network. *Sensors* **2020**, *20*, 3278. doi:10.3390/s20113278.
24. Wagner, P.; Strodthoff, N.; Bousseljot, R.D.; Kreiseler, D.; Lunze, F.I.; Samek, W.; Schaeffter, T. PTB-XL, a large publicly available electrocardiography dataset. *Scientific Data* **2020**, *7*. doi:10.1038/s41597-020-0495-6.
25. Acar, B.; Koymen, H. SVD-based on-line exercise ECG signal orthogonalization. *IEEE Transactions on Biomedical Engineering* **1999**, *46*, 311–321. doi:10.1109/10.748984.
26. Man, S.; Maan, A.C.; Schalij, M.J.; Swenne, C.A. Vectorcardiographic diagnostic &amp prognostic information derived from the 12-lead electrocardiogram: Historical review and clinical perspective. *Journal of Electrocardiology* **2015**, *48*, 463–475. doi:10.1016/j.jelectrocard.2015.05.002.

27. Young, W.J.; van Duijvenboden, S.; Ramírez, J.; Jones, A.; Tinker, A.; Munroe, P.B.; Lambiase, P.D.; Orini, M. A Method to Minimise the Impact of ECG Marker Inaccuracies on the Spatial QRS-T angle: Evaluation on 1, 512 Manually Annotated ECGs. *Biomedical Signal Processing and Control* **2021**, *64*, 102305. doi:10.1016/j.bspc.2020.102305.
28. Hnatkova, K.; Seegers, J.; Barthel, P.; Novotny, T.; Smetana, P.; Zabel, M.; Schmidt, G.; Malik, M. Clinical value of different QRS-T angle expressions. *Europace* **2018**, *20*, 1352–1361.
29. Mieszczanska, H.; Pietrasik, G.; Piotrowicz, K.; McNitt, S.; Moss, A.J.; Zareba, W. Gender-Related Differences in Electrocardiographic Parameters and Their Association With Cardiac Events in Patients After Myocardial Infarction. *The American Journal of Cardiology* **2008**, *101*, 20–24. doi:10.1016/j.amjcard.2007.07.077.
30. SOTOBATA, I.; RICHMAN, H.; SIMONSON, E.; Fukomoto, A. Sex Differences in the Vectorcardiogram. *Circulation* **1968**, *37*, 438–448. doi:10.1161/01.cir.37.3.438.
31. Chaudhry, S.; Muthurajah, J.; Lau, K.; Xiao, H.B. The effect of ageing on the frontal QRS-T angle on the 12-lead ECG. *British Journal of Cardiology* **2019**. doi:10.5837/bjc.2019.034.
32. Augustauskas, R.; Lipnickas, A.; Surgailis, T. Segmentation of Drilled Holes in Texture Wooden Furniture Panels Using Deep Neural Network. *Sensors* **2021**, *21*, 3633. doi:10.3390/s21113633.
33. Goldberger, A.L.; Amaral, L.A.N.; Glass, L.; Hausdorff, J.M.; Ivanov, P.C.; Mark, R.G.; Mietus, J.E.; Moody, G.B.; Peng, C.K.; Stanley, H.E. PhysioBank, PhysioToolkit, and PhysioNet. *Circulation* **2000**, *101*. doi:10.1161/01.cir.101.23.e215.
34. Orphanidou, C.; Bonnici, T.; Charlton, P.; Clifton, D.; Vallance, D.; Tarassenko, L. Signal Quality Indices for the Electrocardiogram and Photoplethysmogram: Derivation and Applications to Wireless Monitoring. *IEEE Journal of Biomedical and Health Informatics* **2015**, *19*, 832–8. doi:10.1109/jbhi.2014.2338351.
35. Pilia, N.; Nagel, C.; Lenis, G.; Becker, S.; Dössel, O.; Loewe, A. ECGdeli - An open source ECG delineation toolbox for MATLAB. *SoftwareX* **2021**, *13*, 100639. doi:10.1016/j.softx.2020.100639.
36. Dilaveris, P.; Gialafos, E.; Pantazis, A.; Synetos, A.; Triposkiadis, F.; Gialafos, J. The spatial QRS-T angle as a marker of ventricular repolarisation in hypertension. *Journal of Human Hypertension* **2000**, *15*, 63–70. doi:10.1038/sj.jhh.1001129.
37. Bacevicius, J.; Abramikas, Z.; Dvinelis, E.; Audzijoniene, D.; Petrylaite, M.; Marinskiene, J.; Staigyte, J.; Karuzas, A.; Juknevicius, V.; Jakaite, R.; et al. High Specificity Wearable Device With Photoplethysmography and Six-Lead Electrocardiography for Atrial Fibrillation Detection Challenged by Frequent Premature Contractions: DoubleCheck-AF. *Frontiers in Cardiovascular Medicine* **2022**, *9*. doi:10.3389/fcvm.2022.869730.
38. Nigusse, A.B.; Mengistie, D.A.; Malengier, B.; Tseghai, G.B.; Langenhove, L.V. Wearable Smart Textiles for Long-Term Electrocardiography Monitoring—A Review. *Sensors* **2021**, *21*, 4174. doi:10.3390/s21124174.
39. Corporation, B. Bittium OmegaSnap™ ECG Electrodes, 2022. Accessed on: 2022-06-23.
40. Partners, D. Viscero–ECG Vest, 2022. Accessed on: 2022-06-23.
41. Jain, U.; Butchy, A.; Leasure, M.; Covalesky, V.; Mccormick, D.; Mintz, G. 12-Lead ECG Reconstruction via Combinatoric Inclusion of Fewer Standard ECG Leads with Implications for Lead Information and Significance. Proceedings of the 15th International Joint Conference on Biomedical Engineering Systems and Technologies. SCITEPRESS - Science and Technology Publications, 2022. doi:10.5220/0010788600003123.
42. Ribeiro, A.H.; Ribeiro, M.H.; Paixão, G.M.M.; Oliveira, D.M.; Gomes, P.R.; Canazart, J.A.; Ferreira, M.P.S.; Andersson, C.R.; Macfarlane, P.W.; Meira, W.; et al. Automatic diagnosis of the 12-lead ECG using a deep neural network. *Nature Communications* **2020**, *11*. doi:10.1038/s41467-020-15432-4.
43. Hannun, A.Y.; Rajpurkar, P.; Haghpanahi, M.; Tison, G.H.; Bourn, C.; Turakhia, M.P.; Ng, A.Y. Cardiologist-level arrhythmia detection and classification in ambulatory electrocardiograms using a deep neural network. *Nature Medicine* **2019**, *25*, 65–69. doi:10.1038/s41591-018-0268-3.
44. Bousseljot, R.; Kreiseler, D.; Schnabel, A. Nutzung der EKG-Signaldatenbank CARDIODAT der PTB über das Internet. *Biomedizinische Technik/Biomedical Engineering* **1995**, pp. 317–318. doi:10.1515/bmte.1995.40.s1.317.
45. Willems, J.L.; Arnaud, P.; van Bemmel, J.H.; Degani, R.; Macfarlane, P.W.; Zywietz, C. Common standards for quantitative electrocardiography: goals and main results. CSE Working Party. *Methods Inf Med* **1990**, *29*, 263–271.